Cloud Phase Determination Using Ground-Based AERI Observations at SHEBA

D. D. TURNER

Cooperative Institute for Meteorological Satellite Studies, University of Wisconsin—Madison, Madison, Wisconsin, and Pacific Northwest National Laboratory, Richland, Washington

S. A. ACKERMAN

Cooperative Institute for Meteorological Satellite Studies, University of Wisconsin—Madison, Madison, Wisconsin

B. A. BAUM

NASA Langley Research Center, Hampton, Virginia

H. E. REVERCOMB

Cooperative Institute for Meteorological Satellite Studies, University of Wisconsin—Madison, Madison, Wisconsin

P. YANG

Department of Atmospheric Sciences, Texas A&M University, College Station, Texas

(Manuscript received 25 July 2002, in final form 19 December 2002)

ABSTRACT

A new technique for ascertaining the thermodynamic cloud phase from high-spectral-resolution ground-based infrared measurements made by the Atmospheric Emitted Radiance Interferometer (AERI) is presented. This technique takes advantage of the differences in the index of refraction of ice and water between 11 and 19 μm. The differences in the refractive indices translate into differences in cloud emissivity at the various wavelengths, which are used to determine whether clouds contain only ice particles or only water particles, or are mixed phase. Simulations demonstrate that the algorithm is able to ascertain correctly the cloud phase under most conditions, with the exceptions occurring when the optical depth of the cloud is dominated by liquid water ($>$70%). Several examples from the Surface Heat Budget of the Arctic Ocean (SHEBA) experiment are presented, to demonstrate the capability of the algorithm, in which a collocated polarization-sensitive lidar is used to provide insight to the true thermodynamic phase of the clouds. Statistical comparisons with this lidar during the SHEBA campaign demonstrate that the algorithm identifies the cloud as either an ice or mixed-phase cloud approximately 80% of time when a single-layer cloud with an average depolarization above 10% exists that is not opaque to the AERI. For single-layer clouds having depolarization of less than 10%, the algorithm identifies the cloud as a liquid water cloud over 50% of the time. This algorithm was applied to 7 months of data collected during SHEBA, and monthly statistics on the frequency of ice, water, and mixed-phase clouds are presented.

1. Introduction

Clouds play an important role in the energy balance of the earth because of their absorption and scattering of solar and infrared radiation. The degree to which the radiation is modulated depends on the thermodynamic phase, size, and shape of the cloud particles, because these dictate the single-scattering properties of the particles. Determining the phase of the cloud particles (i.e., whether they are liquid water or ice) is a prerequisite to specifying the optical and microphysical properties, because an incorrect phase assessment can lead to errors in the estimates of the single-scattering properties. These errors in turn lead to errors in the modeled radiative flux. For example, an incorrect determination of cloud phase can result in large (20%–100%) errors in the effective radius of the cloud particles and optical depth, which translate into errors in the downwelling longwave and shortwave fluxes of 5%–20% (Key and Intrieri 2000).

Several methods exist for determining the phase of clouds from remote sensing measurements. The simplest method is to specify phase based upon the cloud bound-

Corresponding author address: Dr. David D. Turner, CIMSS/University of Wisconsin—Madison, 1225 West Dayton Street, Madison, WI 53706.
E-mail: dturner@ssec.wisc.edu

ary temperature directly calculated from infrared radiance observations (Rossow and Schiffer 1999). Other investigators have taken advantage of the differences in the refractive indices of ice and water as a function of wavelength to determine cloud phase. For example, Strabala et al. (1994) used observations at 8.5, 11, and 12 μm to ascertain cloud phase, where the absorption coefficient of ice is larger than that of water at 11 and 12 μm but is nearly identical at 8.5 μm. Key and Intrieri (2000) modified the trispectral infrared method of Strabala et al. (1994) by using observations at 3.7 μm, in addition to using the observations at 11 and 12 μm from the Advanced Very High Resolution Radiometer (AVHRR) to determine cloud phase because the AVHRR does not have an 8-μm channel. Baum et al. (2000) extended the trispectral method by using the Moderate Resolution Imaging Spectroradiometer (MODIS) Airborne Simulator (MAS) observations at 0.65, 1.63, and 1.90 μm, in addition to using observations at 8.5, 11, and 12 μm to ascertain cloud phase. Knap et al. (2002) have built upon the work of Pilewskie and Twomey (1987a,b) to use reflectivity observations at 1.64 and 1.70 μm to determine cloud phase. All of these methods utilized spectral regions in which the absorption coefficient of ice was either larger than or the same as that of liquid water. However, Daniel et al. (2002) recently developed a technique to retrieve cloud phase from spectrally resolved observations at 850–1050 nm, in which the ice absorption is larger than that of liquid water for a portion of the band and less than that of liquid water in another portion of the band. This technique, along with some of the other methods (Key and Intrieri 2000; Baum et al. 2000; and Knap et al. 2002), utilizes channels that have a significant shortwave component and are dependent on viewing and solar zenith angles. Therefore, these techniques are restricted to daytime only and are not useful during the polar winter.

Accurate determination of cloud phase, and in particular the identification of mixed-phase clouds, is perhaps most critical in the Arctic. The Arctic serves as a heat sink for the earth (Nakamura and Oort 1988), because the outgoing longwave flux is much larger than the incoming solar flux when averaged over a year. However, as indicated earlier, clouds greatly modulate the radiative budget, and Curry et al. (1996) have identified cloud phase as being one of the primary unknowns in the Arctic. The presence of highly reflective snow and ice, together with the persistent temperature inversion that exists much of the year, hampers the ability to determine the cloud phase from passive remote sensors.

Active remote sensors, such as lidars (e.g., Sassen 1991) and cloud radars (e.g., Sekelsky and McIntosh 1996) that are polarization sensitive, can be used to determine cloud phase. The phase is determined by analyzing the change in the polarization of the backscattered energy that is induced by the shape of the cloud particles relative to its original polarization. Spherical particles, such as suspended liquid water drops, induce very little change in the polarization of the electromagnetic wave (typically on the order of 3%–7%), while ice crystals (because of their more complicated shapes) can result in a significant change in the polarization.

The motivation behind this work is to develop an algorithm to determine cloud phase above the Department of Energy's (DOE) Atmospheric Radiation Measurement (ARM) Program Cloud and Radiation Testbed (CART) site at Barrow, Alaska (71.3°N, 156°W). This site was established in the autumn of 1997, and has been collecting a wide range of atmospheric data since its inception. Two of ARM's scientific objectives for the Barrow site are to improve the treatment of the radiative effects of mixed-phase and ice phase clouds, and to improve the description of the cloud microphysical properties and how they are influenced by atmospheric thermodynamics and aerosol characteristics (Stamnes et al. 1999). However, while the site has both a micropulse lidar (Campbell et al. 2002) and a millimeter wave cloud radar (Moran et al. 1998), neither are polarization sensitive. Therefore, we desired to use the other remote sensors at the ARM site to determine the phase of the clouds. The Atmospheric Emitted Radiance Interferometer (AERI), which is part of the suite of instruments at the Barrow site, measures downwelling radiance at high spectral resolution. Our approach is to modify the Strabala et al. (1994) technique to use ground-based AERI data to ascertain cloud phase.

The organization of this paper is as follows. Section 2 provides an overview of the instrumentation used in this study. The theory, approach, and the simulations are presented in section 3. Several case studies are presented in section 4, wherein the phase determination results from the AERI deployed as part of the Surface Heat Budget of the Arctic Ocean (SHEBA) project (Uttal et al. 2002) are compared with profiles of depolarization from a collocated polarization-sensitive lidar. Section 5 discusses a longer, statistical comparison of the AERI-based algorithm with the lidar observations, and monthly statistics on cloud phase as determined from this algorithm are presented. The summary and conclusions are presented in section 6.

2. Instrumentation

The AERI instrument developed for the ARM Program (Revercomb et al. 1993) was an outgrowth of the High-Resolution Interferometer Sounder (HIS) program at the University of Wisconsin (Smith et al. 1993). The AERI is a passive, fully automated, ground-based infrared interferometer. It employs a commercially available interferometer (Michelson series MR100 from Bomem, Inc., of Quebec City, Quebec, Canada[1]), which

[1] Mention of commercial products does not imply endorsement by the U.S. Department of Energy or its contractors.

results in a maximum unapodized spectral resolution of $\sim$0.5 cm^{-1}. The output from the interferometer is directed to a pair of detectors in a ''sandwich'' configuration to give the instrument the spectral coverage that is desired. The sandwich configuration consists of a shortwave InSb detector stacked in front of a photoconductive HgCdTe detector, which views the longwave signal via transmission through the InSb detector. These detectors require cooling, and a solid-state Stirling cooler has been employed for this purpose. The InSb detector is sensitive to radiation between 3.3 and 5.5 μm (3000–1800 cm^{-1}), while the HgCdTe detector used in the standard AERIs is used to sense radiation from 5.5 to 19 μm (1800–520 cm^{-1}). The longwave detectors used in the AERI Extended Range (AERI-ER) systems have been chosen to extend the spectral range beyond 19 μm to observe radiation from 5.5 to 25 μm for deployment in the Arctic. This extended range permits the AERI-ER to observe downwelling radiance in the rotational water vapor band from 18 to 25 μm, which becomes transparent at the low water vapor burdens in the Arctic. However, this modification results in slightly higher noise performance in the main atmospheric window from 8 to 13 μm for the AERI-ER systems, as compared with a standard AERI.

The calibration goal for the AERI systems is to achieve an absolute calibration accuracy of better than 1% of the ambient radiance (Revercomb et al. 1993). To achieve this accuracy, the AERI instruments view two well-characterized calibration sources (Minnett et al. 2001) between each sky dwell period via a rotating scene mirror. A typical measurement cycle is a 3-min sky dwell period followed by 2-min dwell periods at each of the calibration sources, resulting in an approximate 8-min temporal resolution. These sources are high-emissivity (greater than 0.995) blackbody cavities that contain very accurate [National Institute of Standards and Technology (NIST) traceable] temperature sensors. The two blackbodies are identical in design, with one kept at 60°C while the other is allowed to fluctuate along with the ambient temperature. The spectra from the blackbodies, together with their measured temperatures, are used to calibrate the scene-view radiance, following Revercomb et al. (1988).

To apply our phase determination algorithm (which is described in section 3) to the AERI observations, the cloud emissivity must be calculated. The emissivity calculation requires a clear-sky radiance spectrum to be determined, which can come from either a temporally close observed sample or via a calculation. Because stratus clouds are quite frequent and persistent in the Arctic, we use the line-by-line radiative transfer model (LBLRTM; Clough et al. 1992; Clough and Iacono 1995) to provide the clear-sky spectrum, and, thus, the residuals between these calculations and the AERI observations during clear-sky scenes need to be quantified and evaluated. Tobin et al. (1999) used cloud radar and lidar data to identify 62 clear-sky scenes during SHEBA, from which an adjustment to the foreign continuum between 16 and 25 μm was made. Using these same scenes, the residuals were evaluated between 8 and 20 μm, and a persistent $\sim$1 mW (m^2 ster cm^{-1})$^{-1}$ spectrally flat bias was found in the 8–13-μm region, with the observation from the AERI being consistently warmer. Radiosondes are known to have a dry bias and considerable variability in their calibration (e.g., Wang et al. 2002; Turner et al. 2003), but increasing the water vapor used in the calculation by a factor of 2 does not explain the residual. Also, large perturbations to the self-broadened and foreign-broadened water vapor continuum coefficients do not explain the residuals. It is possible that there is something unresolved in the AERI's real-time calibration that would explain this residual, or perhaps there is a small atmospheric contribution from blowing snow or clear-sky ice precipitation that was unaccounted for. This bias is currently unexplained, and, thus, it is subtracted from the AERI observations before cloud emissivity is calculated.

An AERI-ER system was deployed as part of the SHEBA experiment (Uttal et al. 2002). During this multiagency, interdisciplinary experiment, the Canadian icebreaker *Des Grosilliers* was frozen into the perennial ice pack from November 1997 to August 1998, serving as a floating scientific research station to enhance the understanding of the thermodynamic coupling among the atmosphere, the sea ice, and the ocean (Uttal et al. 2002). During this experiment, a polarization-sensitive lidar was deployed near the AERI. The National Oceanic and Atmospheric Administration (NOAA) Environmental Technology Laboratory's Depolarization and Backscatter Unattended Lidar (DABUL) is a compact, autonomous lidar system, designed to produce research-quality measurements of backscatter and depolarization ratio measurements from clouds and aerosols (Alvarez et al. 1998). The DABUL is a hardened and portable instrument that can be placed in a variety of field locations with minimal infrastructure. The system transmits pulses of 523-nm light from a doubled Nd:YLF laser. Low-pulse energies are used (less than 40 μJ per pulse), and the outgoing laser energy is expanded by the shared transmit/receive telescope (which has a diameter of 30 cm) to assure eye safety. A high-pulse repetition rate (over 1 kHz) and pulse averaging are used to achieve the required signal-to-noise ratio.

The DABUL's receiver only detects light for a single linear polarization, but the polarization of the outgoing light is rotated on alternating pulses by a Pockels cell. This allows both copolarized and cross-polarized components of the backscatter to be observed. The depolarization ratio (the ratio of the cross- to copolarized signal as a function of range) provides information on cloud particle phase. The nominal vertical and temporal resolution of the DABUL is 30 m and 5 s, but temporal and vertical resolution can be traded off to improve the signal-to-noise ratio in lidar data. The DABUL data used

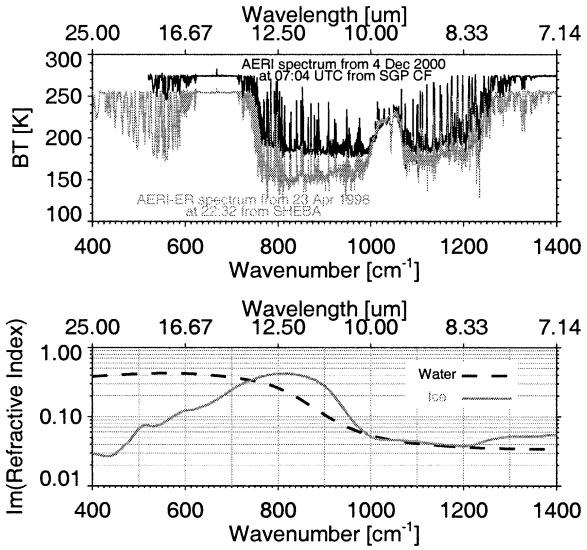

FIG. 1. (top) Example of AERI brightness temperature spectra for clear-sky, dry conditions at the SGP (1.2 cm PWV) and SHEBA (0.33 cm PWV), and (bottom) the imaginary refractive index of water and ice.

in this paper had temporal and vertical resolutions of 10 min and 30 m, respectively.

Depolarization ratio data, such as that collected by the DABUL, provide one way to ascertain the phase of detected cloud particles, up to the limit of signal attenuation. Spherical particles, such as liquid water drops, typically induce little to no depolarization in the forward or backward scattering directions, with values typically less than a few percent, yet have strong total backscatter returns. However, strong multiple scattering by the cloud droplets can induce an increasing depolarization ratio with range, because the scattering by spherical particles at angles other than 0° or 180° does induce some depolarization, which can be multiple scattered back into the field of view of the lidar. These cases can usually be identified by a very strong backscatter signal. Nonspherical particles, such as ice crystals, typically result in large depolarization ratios (between 10% and 50%), depending on such factors as the ice crystal habit, size distribution, and particle orientation (Sassen 1991). A special case occurs, however, if the ice crystals are coated with water or if water droplets coexist in the same volume as ice crystals (i.e., a mixed-phase cloud), because the depolarization ratio is smaller than that of pristine ice crystals of the same habit. Therefore, there is not a single depolarization threshold that can be used to unambiguously separate ice-only clouds from mixed-phase clouds.

3. Approach

a. Cloud emissivity

In the infrared, the imaginary part of the refractive indices of liquid water (Downing and Williams 1975) and ice (Warren 1984) vary dramatically with wavelength, as shown in Fig. 1. The single-scattering properties of the cloud particles are determined by the complex index of refraction ($m = m_r - im_i$), as well as the size distribution and shape of these particles. The absorption coefficient κ, which describes the cloud absorption and emission, is a function of wavelength λ and m_i given by (Bohren and Huffman 1983)

$$\kappa = 4\pi \frac{m_i}{\lambda}. \quad (1)$$

Many studies (e.g., Baum et al. 2000; Strabala et al. 1994) use the differences between ice and water absorption at 12 μm (where the ice is more absorbing than liquid water) together with observations at 8.5 μm (where ice and liquid water absorption is approximately equal). However, as shown in Fig. 1 and Table 1, the absorption by liquid water is significantly stronger than that of ice between 18 and 25 μm, and, thus, using data from this region together with observations at 8.5 and 12 μm offers more information for accurate phase determination. The ground-based AERI-ERs, as well as the standard AERIs at the other ARM CART sites, such as in the Southern Great Plains (SGP), make measurements at these longer wavelengths. Thus, the AERIs can

TABLE 1. The center wavelength, wavenumber range, imaginary indices, and absorption coefficients of water and ice in each of the microwindows that were evaluated for phase determination from the AERI. The optical constants for liquid water and ice are from Downing and Williams (1975) and Warren (1984), respectively.

Center wavelength (μm)	Wavenumber range (cm^{-1})	Ice m_i	Water m_i	Ice κ	Water κ
20.13	495.5–498.0	0.0629	0.4170	0.0393	0.2603
18.84	529.9–531.5	0.0723	0.4251	0.0482	0.2835
17.85	558.5–562.0	0.0877	0.4270	0.0618	0.3006
12.02	830.0–834.5	0.4142	0.2049	0.4330	0.2142
11.83	843.0–847.5	0.4011	0.1835	0.4260	0.1949
11.44	873.2–875.5	0.3519	0.1382	0.3866	0.1518
11.09	898.5–904.7	0.2739	0.1053	0.3104	0.1193
9.12	1095.0–1098.2	0.0442	0.0413	0.0609	0.0569
8.97	1113.5–1116.1	0.0425	0.0402	0.0595	0.0562
8.12	1231.3–1232.2	0.0413	0.0355	0.0639	0.0550

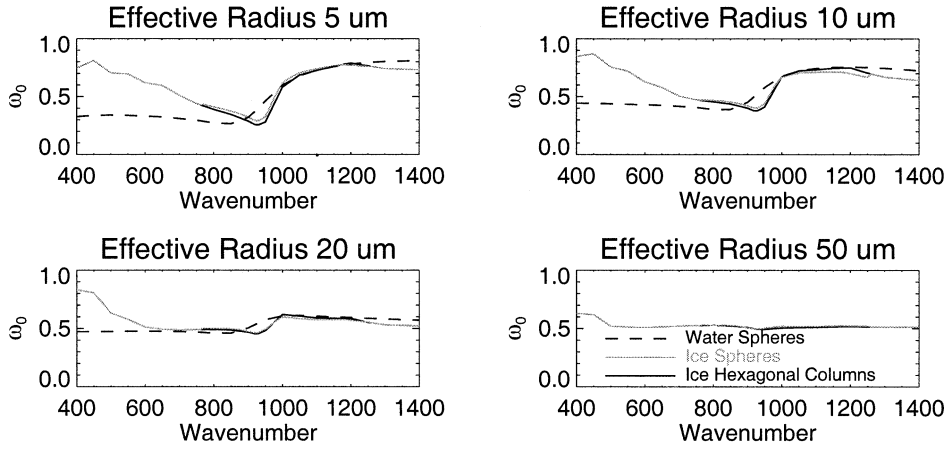

FIG. 2. Comparison of ω_0 as a function of wavelength for spherical water particles, spherical ice particles, and hexagonal ice particles for four different sizes. Note the good agreement between the two different ice habits for these effective radii.

be used to ascertain cloud phase provided that the water vapor burden is not too large, thereby causing the 18–25 μm to become opaque.

When computing single-scattering properties for ice particles, the particles have typically been assumed to be spherical to allow the properties to be computed from Mie theory, which is simple and well established. In the last several years, new computational procedures have been developed that allow these scattering properties to be calculated for more realistic particle shapes (e.g., Yang and Liou 1996; Mishchenko et al. 2000; Baran and Havemann 1999; Yang et al. 2000; Yang et al. 2001). Using the finite-difference time-domain (FDTD) procedure, an improved geometric optics method, and the stretched scattering potential method, Yang et al. (2001) have computed single scattering properties for hexagonal columns in the 8–13-μm region. A comparison of single-scatter albedo ω_0 computed for the columns from this method versus spherical particles from Mie theory for different effective radii is presented in Fig. 2. For this comparison, a gamma size distribution was assumed, which fit the Arctic data collected by Lawson et al. (2001; Fig. 3) during the First International Satellite Cloud Climatology Project (ISCCP) Regional Experiment (FIRE) Arctic Cloud Experiment (ACE). Note the relatively good agreement between the two ice habits for this parameter. This agreement may be due to the fact that the aspect ratio of the hexagonal columns is 1 for particles less than 40 μm, and slowly changes from unity as the size increases (Yang et al. 2001). In this paper, the ice particles will be assumed to be hexagonal crystals.

To determine the cloud phase, a variety of tests are applied to the spectral emissivity of the cloud. Using

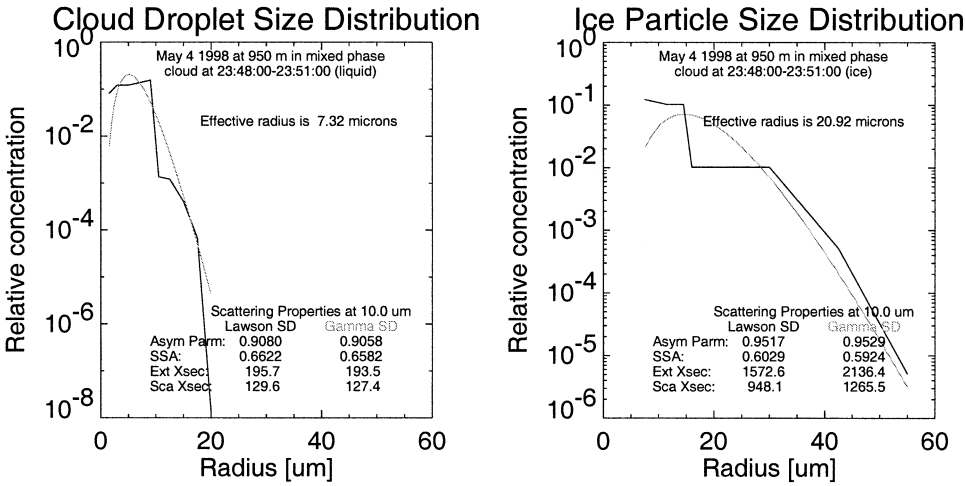

FIG. 3. Size distribution of liquid water and ice particles in a mixed-phase cloud as observed by the CPI flown on the C-130 aircraft during FIRE ACE. The gamma distribution with a matching effective radius is also shown.

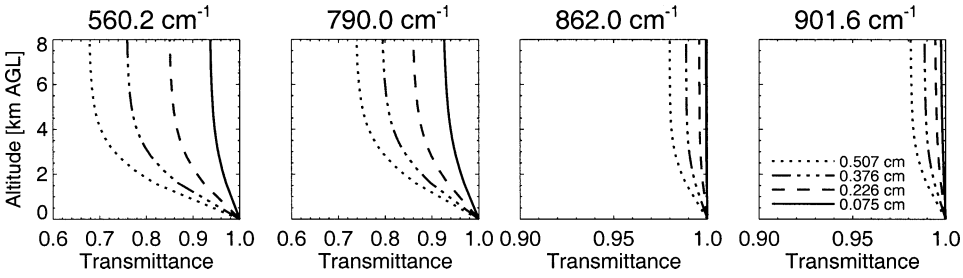

FIG. 4. Level-to-surface transmission profiles for four different microwindows. Each curve corresponds to a different amount of precipitable water vapor. The standard subarctic winter profile was used for these calculations.

cloud emissivity minimizes the impact of changing water vapor burdens on the cloud detection algorithm. For downwelling radiation where a single, infinitesimally thin cloud exists and assuming that the cloud reflectance r_c is zero, the radiative transfer equation is given by

$$R^{\downarrow} = \int_{p_s}^{p_c} B[T(p)]\frac{d\Im}{d\ \ln p}\, d\ \ln p + \Im_{p_c}^{p_s}\varepsilon_c B(T_c) + (1 - \varepsilon_c)\int_{p_c}^{0} B[T(p)]\frac{d\Im}{d\ \ln p}\, d\ \ln p, \quad (2)$$

where ε_c is the cloud emissivity, B is the Planck function, $T(p)$ is the ambient temperature profile, T_c is the effective cloud temperature, p_c is the cloud-base pressure, p_s is the surface pressure, $\Im$ is the transmission from the surface to level p, and $\Im_{p_c}^{p_s}$ is the transmittance from p_c to p_s. The frequency dependence on all quantities other than T_c, T, and p is understood. The clear-sky downwelling radiance is given by

$$R_{\text{clr}}^{\downarrow} = \int_{p_s}^{0} B[T(p)]\frac{d\Im}{d\ \ln p}\, d\ \ln p = \int_{p_s}^{p_c} B[T(p)]\frac{d\Im}{d\ \ln p}\, d\ \ln p + \int_{p_c}^{0} B[T(p)]\frac{d\Im}{d\ \ln p}\, d\ \ln p, \quad (3)$$

and, thus,

$$R^{\downarrow} - R_{\text{clr}}^{\downarrow} = \varepsilon_c\left\{\Im_{p_c}^{p_s}B(T_c) - \int_{p_c}^{0} B[T(p)]\frac{d\Im}{d\ \ln p}\, d\ \ln p\right\}. \quad (4)$$

Because most of the water vapor is near the surface, the level-to-surface transmittance term $\Im_{p_c}^{p_s}$ typically can not be assumed to be unity. However, depending on the height of the cloud, the wavelength of radiation, and the amount of water vapor, we often can assume that $\int_{p_c}^{0} B[T(p)]d\Im/d\ \ln p\ d\ \ln p \approx 0$. This assumption allows us to express the cloud emissivity, computed from downwelling radiance observations at the surface, as

$$\varepsilon_c = \frac{R^{\downarrow} - R_{\text{clr}}^{\downarrow}}{\Im_{p_c}^{p_s}B(T_c)}. \quad (5)$$

The level-to-surface transmission term complicates the derivation of the cloud emissivity. In the Arctic, this term is very close to unity for channels between 8 and 13 μm because of the very low amounts of water vapor present and, thus, can be assumed to be 1. This term cannot be set to unity in the 17–25-μm region because of the strength of the water vapor absorption in this spectral region. Figure 4 provides some example profiles of the term in several microwindows for a range of water vapor burdens. The level-to-surface transmission term is computed from radiosonde data; radiosondes were launched every 6 h during SHEBA.

b. Simulations

Simulations were used to investigate the ability to infer cloud phase using cloud emissivity spectra computed from downwelling high spectral resolution radiance observations. Microwindows were chosen at these spectral locations to avoid line absorption by water vapor and other trace gases, and calculations were made at these wavelengths. The locations of the microwindows, together with the refractive indices and absorption coefficients, are given in Table 1. The gaseous optical depths were calculated using the LBLRTM, which used the high-resolution transmission (HITRAN) 2000 spectroscopic database and the Clough–Kneizys–Davies (CKD) water vapor continuum model, version 2.4. Note that this continuum model includes the modification to the foreign continuum in the 17–26-μm region (Tobin et al. 1999). These optical depths, together with single-scattering properties of all-water, all-ice, and mixed-phase clouds, supplied input into Discrete Ordinates Radiative Transfer (DISORT) (Stamnes et al. 1988) and the downwelling radiance was computed.

Mixed-phase clouds are modeled in three ways. The first two methods consist of modeling the cloud as adjacent cloud layers, with the ice layer directly above the water layer in the first, and the water layer directly above the ice layer in the second. In both cases, the temperature of both layers is the same. The third type of mixed-

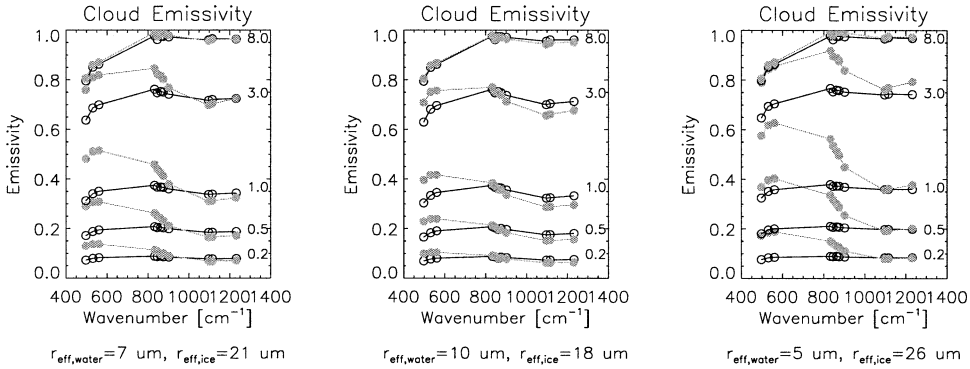

FIG. 5. Cloud emissivity spectra (computed in each of the microwindows identified in Table 1). Black curves with open circles are ice-only clouds, and curves with solid gray circles are liquid water clouds. The effective sizes of the particles are given below each plot. For each particle size, calculations were made for optical depths 0.2, 0.5, 1.0, 3.0, and 8.0 (these are indicated in the right of each plot). Note how the slope of the emissivity in the 800–900-cm^{-1} region is different for ice and water clouds, as well as the change in the emissivity at 500–570 cm^{-1} as compared with that at 800–900 cm^{-1} for ice and water clouds.

phase cloud assumes that the ice and water particles are uniformly mixed together in the same volume, and that the single-scattering properties are combined linearly in τ as in Sun and Shine (1995):

$$\tau_m = \tau_i + \tau_w, \tag{6}$$

$$\omega_{0,m} = (\tau_i \omega_{0,i} + \tau_w \omega_{0,w})/\tau_m, \tag{7}$$

$$g_m = (\tau_i \omega_{0,i} g_i + \tau_w \omega_{0,w} g_w)/(\tau_m \omega_{0,m}), \tag{8}$$

$$p_m = (\tau_i \omega_{0,i} p_i + \tau_w \omega_{0,w} p_w)/(\tau_m \omega_{0,m}), \tag{9}$$

where p denotes the scattering phase function and i, w, and m represent ice, water, and mixed-phase clouds, respectively. For this work, the scattering function was approximated by the Henyey–Greenstein function.

c. Algorithm description

A series of simulations for different particle size distributions were used for the liquid- and ice-only clouds over a range of optical depths. The emissivity spectra for some of these runs are shown in Fig. 5. Several features become apparent upon examining these spectra. First, the slope of the emissivity from 800 to 900 cm^{-1} (11–12 μm) is much steeper for liquid-only clouds than for ice-only clouds, especially for optical depths less than approximately 6. Also, because the absorption of liquid water is much stronger than that of ice in the 18–25-μm window, the emissivity of liquid water clouds is significantly larger than that of ice clouds in this spectral region.

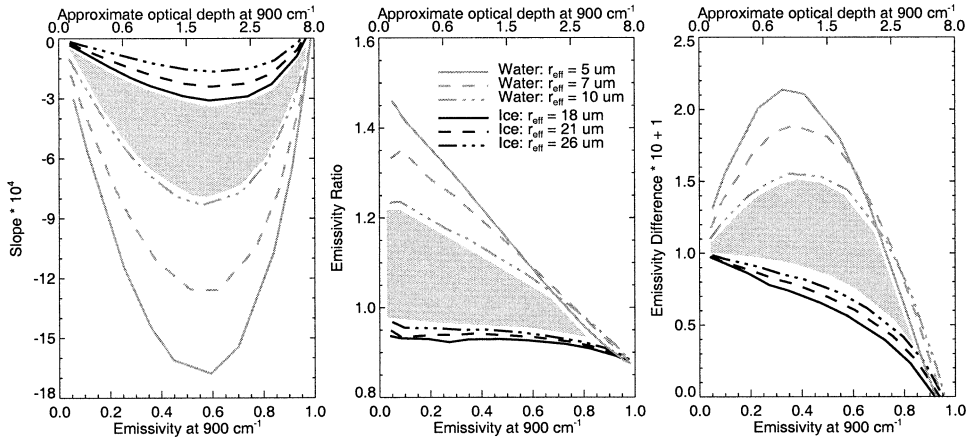

FIG. 6. (left) The slope of the emissivity between 800 and 900 cm^{-1} for ice (black lines) and water (gray lines) clouds of different effective radii. The gray region in the middle denotes values that are associated with mixed-phase clouds. The values above and below this region are identified with ice and liquid clouds, respectively. (middle) A similar plot for the ratio of the mean emissivity for 17–19 μm to the mean emissivity for 11–12 μm. (right) A similar plot for the difference of the mean emissivity for 17–19 μm and the mean emissivity for 11–12 μm. The results from these three tests are combined to yield the phase determination from the high-spectral-resolution emissivity data.

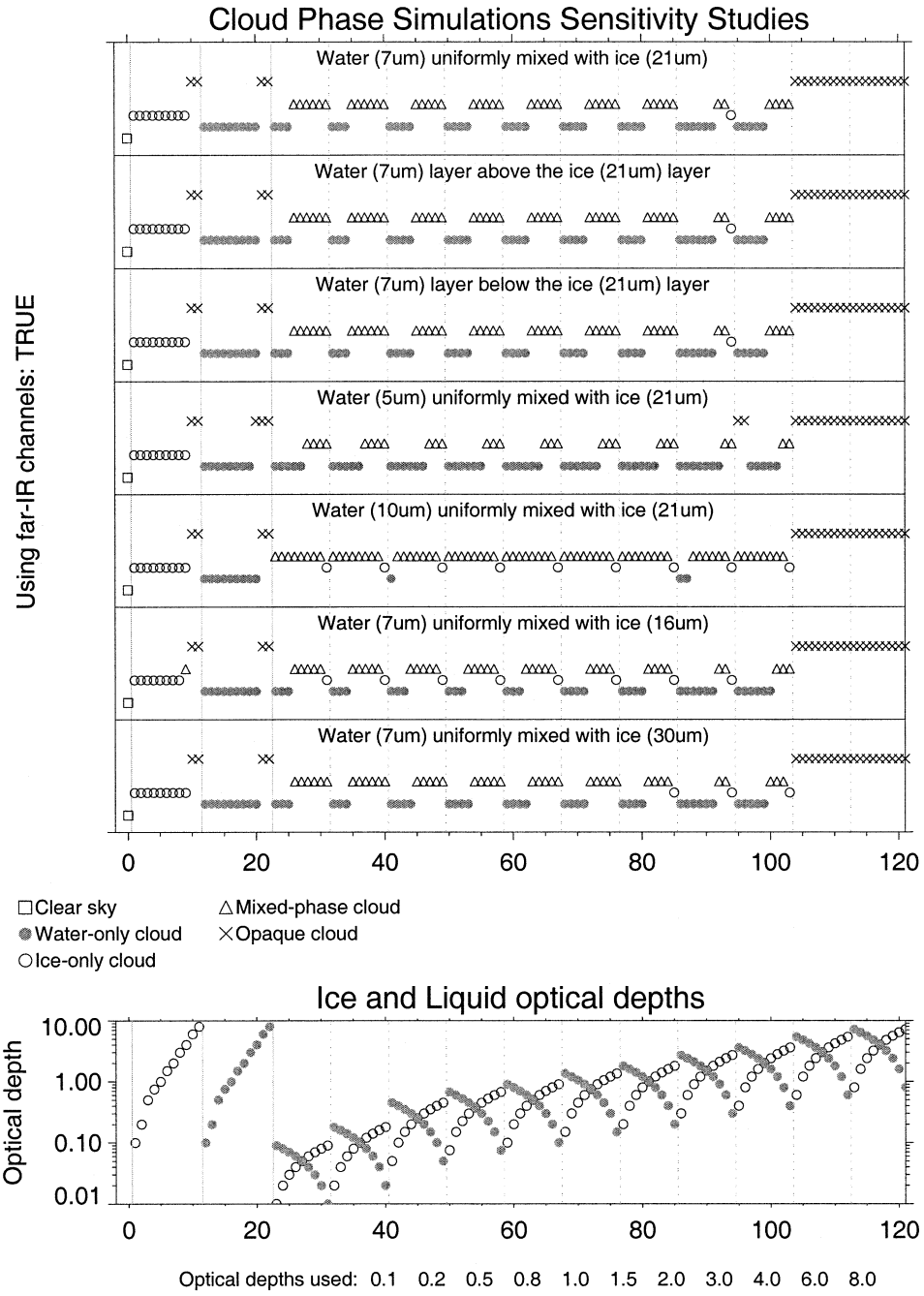

FIG. 7. Sensitivity of the phase determination algorithm on the layer structure as well as cloud particle size. See the text for details.

These simulations were used to develop three tests to determine cloud phase. These tests are depicted graphically in Fig. 6. The first test (Fig. 6, left-hand side) determines the phase by looking at the slope of the emissivity in the four microwindows in the 11–12-μm region. If the slope is significantly negative, then the cloud is identified as a liquid water cloud; if the slope is close to zero, then the cloud is identified as an ice-only cloud. Clouds whose slope lands in the intermediate region (identified in gray) are classified as mixed-phase clouds. The second test (Fig. 6, center) uses the ratio of the mean emissivity from 17–19 μm to the mean emissivity in the 11–12-μm region. If this ratio is below approximately 1.0 (as shown by the curve in Fig. 6), the cloud is classified as an ice cloud, but if the ratio is quite large, then it is identified as a liquid cloud. Again, the intermediate region in gray is associated with mixed-phase clouds. This test is quite sensitive to clouds

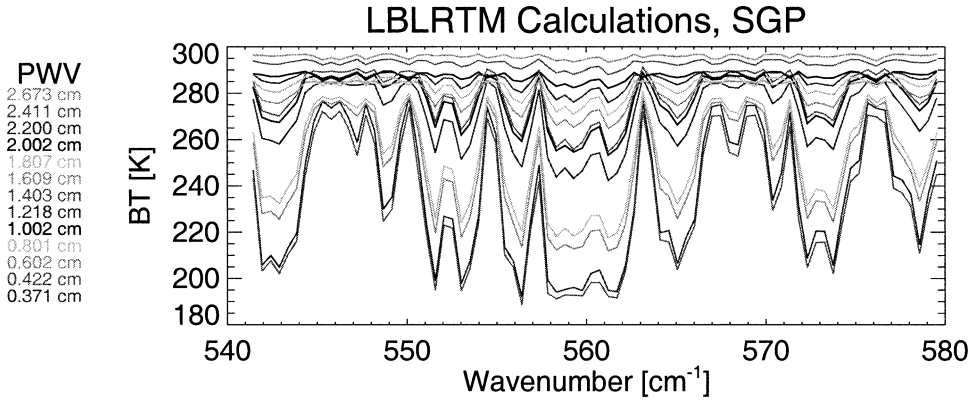

FIG. 8. Downwelling brightness temperature calculations for a range of PWV at the ARM SGP site. All of these calculations are for clear sky. Note how the 17.8-μm microwindow (558–562 cm^{-1}) closes as the PWV increases.

with small optical depths (and, hence, small values of emissivity at 900 cm^{-1}). The third test (Fig. 6, right-hand side) looks at the difference in the mean emissivity between 17–19 and 11–12 μm. This test provides improved sensitivity to clouds of intermediate optical depth. All three tests become insensitive to cloud phase when the optical depth of the cloud becomes larger than approximately 6. Clouds that have emissivity values at 900 cm^{-1} over 0.95 are flagged as opaque. The results from the three tests are combined democratically to yield the final determination of the cloud phase: that is if any two tests agree on the phase, the cloud is classified as such, and if all three tests disagree then the cloud is specified as ambiguous.

To evaluate this phase determination algorithm, a simulation consisting of various different clouds was performed, where the optical depth of the clouds ranged from 0.1 to 8. For each optical depth, the fraction of the optical depth that was due to liquid water ranged from 0.0 (all-ice cloud) to 1.0 (all–liquid water cloud) in increments of 0.1. The simulated dataset was arranged so that the first case was a clear-sky case, the next 11 cases were all ice-only clouds where the optical depth was slowly increased, followed by 11 cases of water-only clouds for the same set of optical depths. The next 11 segments each have 9 cases, where the total optical depth for each segment is fixed (starting from 0.1, 0.2, and 0.5, up to 8.0) and the fraction of the optical depth associated with ice starts at 0.1 and increases to 0.9 in increments of 0.1. The ice and liquid optical depths are shown in the bottom of Fig. 7. The temperature and water vapor profiles for this example are from a SHEBA sounding on 25 April 1998, and the precipitable water vapor amount is 2.44 mm. The clouds are placed between 600 and 700 m where the temperature is -16°C. The effective radii of the size distributions for the cloud particles are 7 and 21 μm for liquid and ice, as suggested by Cloud Particle Imager (CPI) observations in Fig. 3 (Lawson et al. 2001). The upper panel in the upper plot shows the results of the phase detection algorithm. When the cloud is composed of only ice particles, the phase is determined correctly for all optical depths less than 5, and similarly for clouds that consist only of liquid water particles. For optical depths greater than 5, the clouds are flagged as opaque by the algorithm. For the mixed-phase clouds, the algorithm correctly classifies the cloud as mixed phase for the entire range of total optical depths, as long as the fraction of the optical depth due to the ice particles is significant (i.e., greater than ~40%). When the fraction of the optical depth due to liquid water is greater than ~60%–70%, the cloud is misclassified as a liquid water cloud.

Sensitivity studies were used to evaluate the algorithm performance further. These results are also presented in Fig. 7. For the same simulation setup as before, the composition (layering or effective particle size) of the mixed-phase cloud was altered. Using the results from the top panel in Fig. 7 as the baseline, the results of the algorithm due to changes in layering and particle size were evaluated. In many mixed-phase clouds, the particles are not uniformly mixed in a volume (this is inherently unstable because of the difference in the saturation vapor pressure of ice and water when both are at the same temperature), but, rather, the cloud has a two-layer structure with a liquid water layer directly adjacent to an ice layer. These simulations show that as long as both layers have the same temperature, the phase determination algorithm is insensitive to the vertical organization of the particles. The simulations also demonstrate that the algorithm is relatively insensitive to the size of the ice particles. However, the algorithm does show some sensitivity to the size of the water droplets, as would be expected given the series of curves associated with the different-sized water droplets in Fig. 6. If the effective radius of the water droplets is known or can be predicted (e.g., from climatological data), the phase algorithm could be optimized to improve these results. However, the algorithm correctly classifies the majority of the clouds in these simulations.

Critical to the success of this algorithm are the ob-

servations in the 17–20-μm microwindows, where water vapor absorption is stronger in comparison with the microwindows in the 8–13-μm region. Water vapor is concentrated primarily near the surface, and most clouds will generally be above a significant fraction of the total amount of water vapor. Because the AERI is measuring downwelling radiation, there will be some upper limit where the total precipitable water vapor (PWV) is high enough that the 17–20-μm microwindows are effectively closed and, thus, there is little to no sensitivity to clouds. Simulations using data at the ARM site in the SGP, where the PWV has a larger range than the Arctic, demonstrate that there is less than a 30-K brightness temperature difference at 560 cm^{-1} (the center of the 17.8-μm microwindow) and the nearby opaque lines when the PWV is greater than ~1.0 cm (Fig. 8). Therefore, this algorithm should be able to yield cloud phase information for PWV amounts below this threshold. PWV below these amounts are typically found in the Arctic for most of the year with the exception of the summer (Serreze et al. 1995) and during the winter for some midlatitude sites, such as the ARM SGP site.

4. Case studies

The phase determination algorithm was applied to data collected by the AERI-ER at the SHEBA site from November 1997 to May 1998. The collocated DABUL (which was located within 100 m of the AERI) was used to evaluate the validity of the phase determination algorithm. Three case studies on 26, 23, and 21 April are presented to demonstrate the algorithm's ability to ascertain the cloud phase.

To calculate cloud emissivity from an observed AERI spectrum, an estimate of the effective cloud temperature is required. While we could use the cloud boundaries provided by the DABUL along with the temperature profile from the radiosondes (which were launched typically 4 times per day at SHEBA), we chose to use the minimum local emissivity variance (MLEV) method instead (Huang et al. 2001, 2002, manuscript submitted to *J. Appl. Meteor.*). This method retrieves the effective cloud temperature directly from the AERI data in an iterative manner and is independent of cloud boundary information. The basic technique, which is illustrated in Fig. 9, works as follows. A spectral region is chosen that has both weak and strong water vapor absorption lines, such as between 780–800 cm^{-1}, and the emissivity in this region is calculated for a range of realistic cloud temperatures. The effective cloud temperature is the temperature for which the variance in the emissivity is at a minimum.

A relatively simple cloud scene existed on 26 April over the *Des Grosilliers*, which was stationed at 76.00°N, 165.34°W. The winds were primarily westerly at the surface at about 3.5 m s^{-1}, and the surface temperature was approximately −20°C. An upper-air high west of the ice camp helped to prevent thick cirrus clouds from moving over the site. Figure 10 shows that the clear-sky conditions during the beginning of the day gave way to a low, overcast cloud around midday; the cloud descended from approximately 800 to 500 m by the end of the day. These clouds strongly scattered the laser radiation, yet have a small depolarization ratio (less than 10%) and, thus, are considered to be liquid water clouds. The clouds on this day generally had an optically thickness greater than 3, the point at which the laser beam becomes fully attenuated by the cloud as indicated by the decrease in signal to noise above the cloud in

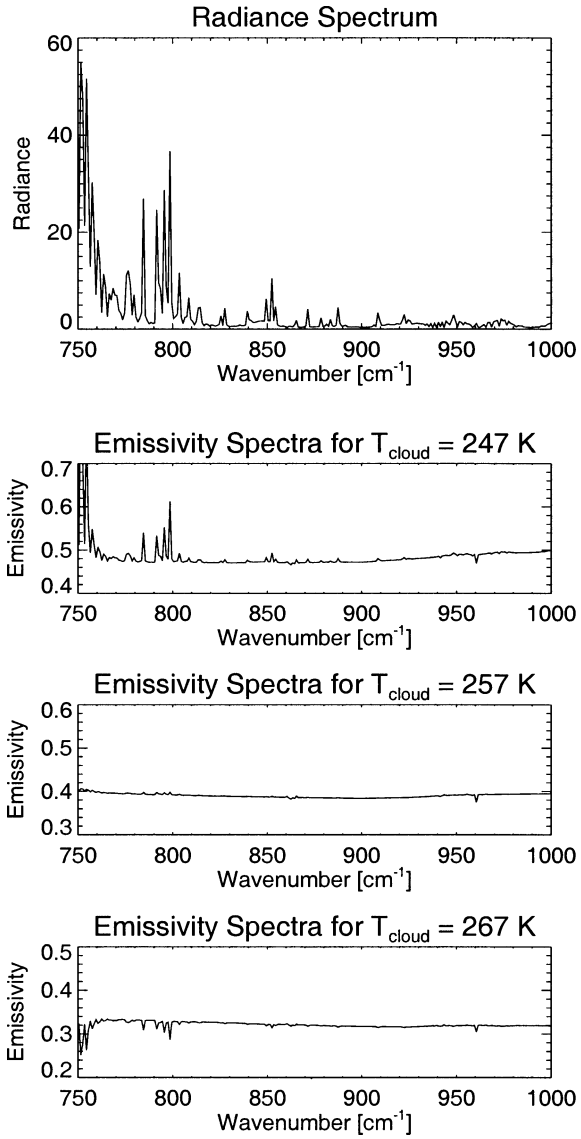

FIG. 9. (top) Typical downwelling radiance observed at the surface by the AERI. Note the strong water vapor absorption lines between 780 and 800 cm^{-1}. The other panels show the emissivity spectra computed using different values for the effective cloud temperature. The line structure is readily apparent in this spectral region in the cases in which T_{cloud} is 247 and 267 K. The MLEV technique looks to minimize the variance in the emissivity in a localized region, resulting in an effective cloud temperature of 257 K.

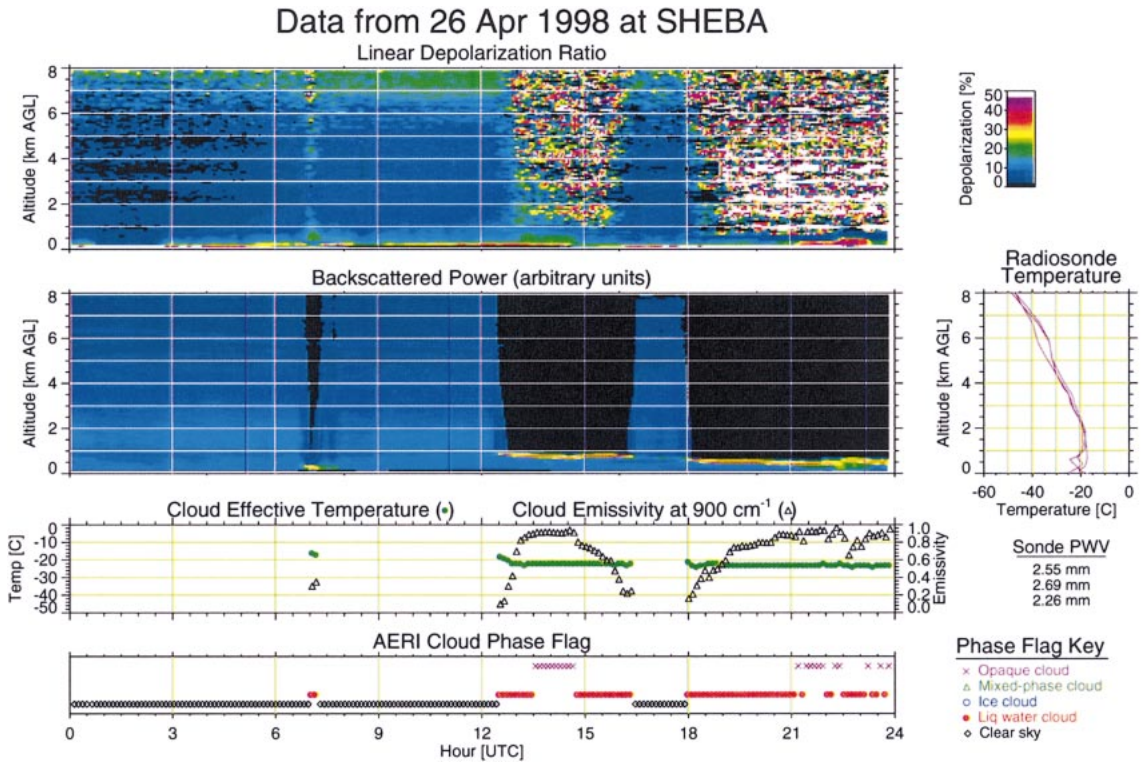

FIG. 10. Time–height plot showing depolarization ratio and backscattered power over the SHEBA ship as observed by the DABUL on 26 Apr 1998. The purple vertical lines on the backscattered power figure indicate the radiosonde launch times, and the temperature profiles from these are shown on the right. The cloud temperature, retrieved using the MLEV technique, along with the emissivity at 900 cm^{-1}, is also indicated. Along the bottom of the image is the output of the AERI phase determination algorithm, color coded to indicate the phase of the clouds. See text for details.

the depolarization ratio. This cloud is correctly classified as a liquid water–only cloud by the AERI phase algorithm, except where the optical depth becomes larger than 5 and the algorithm indicates that the cloud is opaque. Note that the temperature of the cloud retrieved via the MLEV technique is about −21°C from 1300 to 1600 UTC, and about −23°C from 1800 to 2400 UTC, which agrees well with the temperature from the radiosonde profile at the cloud height. The temperatures from the MLEV technique are also very steady about these values, even though the cloud emissivity varies greatly.

A transition in the cloud scene over the SHEBA ship took place on 23 April. A strong surface high started moving over the ice camp from the northwest, heading toward the Beaufort Sea. The resulting winds were northerly at 5–7.5 m s^{-1} and the temperatures remained fairly constant all day. The moving pressure center resulted in the clearing of the midlevel and low-level clouds by midday. The DABUL observations in Fig. 11 show that a cloud system with relatively high depolarization values existed from the beginning of the day until about 1030 UTC, with a few relatively cloud-free periods in between. These images indicate what appear to be precipitation bands of falling ice particles reaching the surface. The AERI was not operating for the first few hours of this day. After it returned to operation, the clouds in this period were classified as being ice-only clouds, and the one clear-sky period from 0515 to 0645 UTC corresponds well with the break in the clouds observed by the DABUL. A second cloud was observed by both systems from 1500 to 1600 UTC. This cloud was classified as a liquid water cloud by the AERI algorithm, which agrees well with the diagnosis from the DABUL, because liquid water clouds have strong backscatter and low depolarization ratios.

On 21 April, the cloud scene was more complicated. A surface high was located in the eastern Beaufort Sea, a small surface low was just northeast of the ship, and a larger low pressure center was far south of the ship along the Asian coast of the Bering Sea. The winds were light and easterly at the surface, while upper-level winds above the ship were from the southwest. Two cloud layers are readily apparent in the DABUL data (Fig. 12). A thick (4–5 km) cloud layer with a base at roughly 2 km was present from about 0900 UTC to the end of the day, with a few breaks in the layer near the end of the day. This layer has a relatively high depolarization ratio, indicating that ice particles are present in this layer. The lower layer at 200 m from approximately 1500 to 2400 UTC (with some temporal gaps) has very low (<10%) depolarization ratios and high backscattered power, which suggest that the scattering

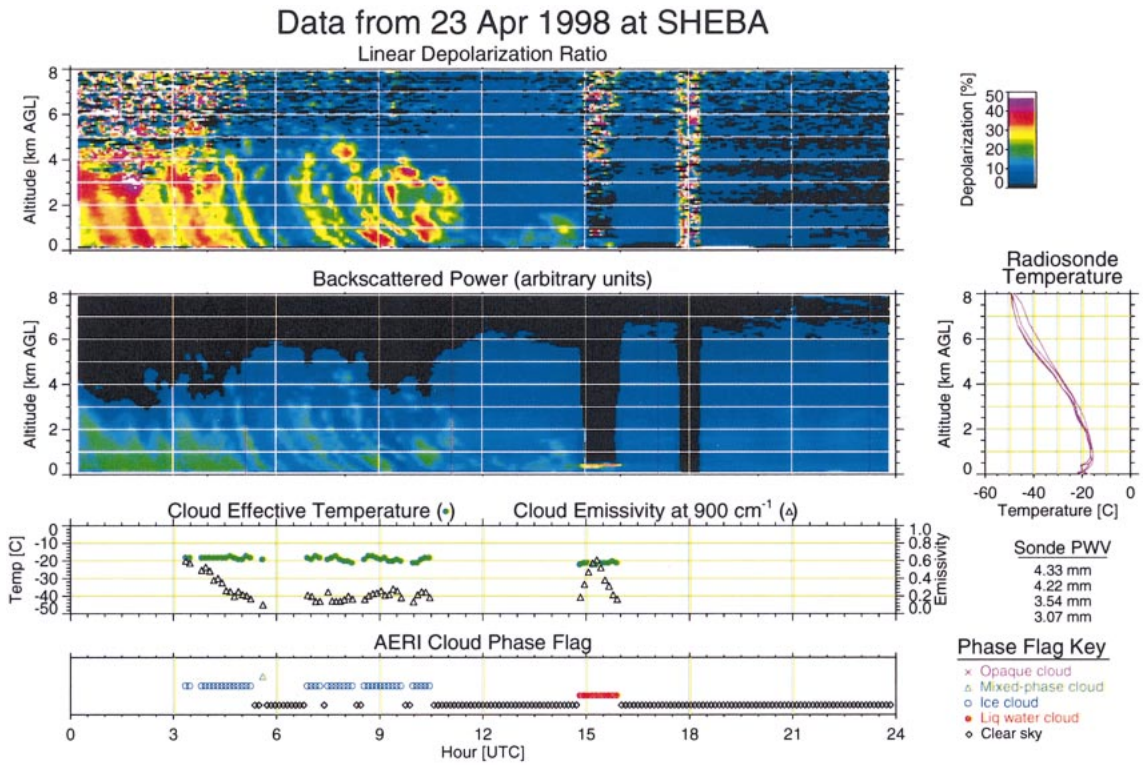

FIG. 11. Same as Fig. 10, but for 23 Apr 1998.

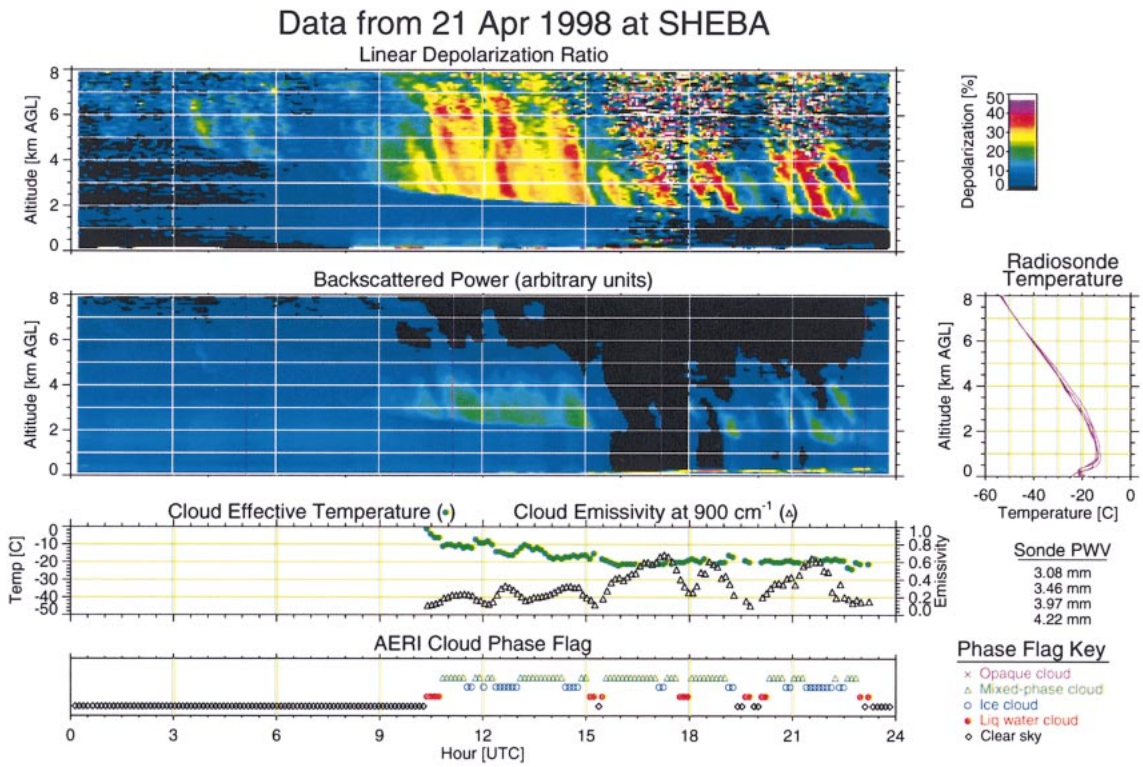

FIG. 12. Same as Fig. 10, but for 21 Apr 1998.

TABLE 2. Number of coincident samples in each category of mean depolarization value reported by the DABUL for single-layer, nonopaque clouds, where F_water, F_mixed, and F_ice are the fractions of the time in each category that the AERI phase determination algorithm reported water, mixed-phase, or ice clouds, respectively.

DABUL depolarization	No. of samples	F_water	F_mixed	F_ice
<10%	3286	51%	19%	26%
10%–30%	1265	28%	27%	45%
>30%	718	8%	21%	71%

TABLE 3. Monthly statistics on the number of hours, and the fraction reported as clear, liquid phase, mixed phase, ice phase, or opaque by the AERI algorithm for 7 months during SHEBA.

Month	Hours	F_clear	F_water	F_mixed	F_ice	F_opaque
Nov	715.6	36%	12%	13%	22%	18%
Dec	722.0	76%	5%	4%	8%	8%
Jan	720.1	63%	8%	5%	5%	19%
Feb	440.9	50%	5%	3%	6%	30%
Mar	740.6	39%	12%	8%	9%	28%
Apr	709.8	32%	11%	10%	22%	26%
May	482.9	16%	32%	8%	14%	31%
Total	4648.2	45%	11%	8%	14%	21%

is due to liquid water particles. The AERI phase algorithm indicates that the upper layer is a mixed-phase cloud from 0900 to 1500 UTC, except for the regions of the most intense depolarization where the AERI algorithm indicated that the cloud was composed of only ice particles (such as between 1230–1300 and 1415–1500 UTC). When there are breaks in this upper layer above the lower-level cloud (i.e., the lower-level cloud is the only cloud layer in the vertical column), the phase algorithm indicates that the lower layer is liquid water, which agrees well with the DABUL observations. When both layers are present simultaneously, the algorithm classifies the scene as mixed phase, because the spectral signature of both ice and liquid water are present.

5. Statistics

While the case studies provide some examples of how the phase algorithm works in particular situations, a more quantifiable evaluation is required before this algorithm could be used to evaluate larger data records that do not have supplemental information on cloud phase (such as data from the ARM Barrow site). The DABUL and the AERI were collocated for most of the SHEBA experiment, and, thus, we can compare the cloud classification from these two systems to indicate when they agree and when they do not. The DABUL data, which were retrieved from the University Corporation for Atmospheric Research's (UCAR's) Joint Office for Science Support (JOSS) archive, were filtered to merge any two cloud layers that were separated by less than 100 m into a single layer. To simplify the analysis between the DABUL and AERI techniques, coincident samples were analyzed only if both methods identified a cloud, the cloud was a single-layer cloud, and the cloud was not opaque as determined by the AERI's algorithm. Approximately 630 h of data met these requirements. While clouds that have depolarization values less than approximately 10% are most likely liquid water clouds, it is not possible to set a threshold to distinguish between ice-only clouds and mixed-phase clouds. Therefore, the results were broken into three categories: clouds that have mean depolarization less than 10%, mean depolarization values between 10% and 30%, and clouds that have a mean depolarization above 30%. In each category, the percentage of time when the AERI reported liquid water, mixed-phase, and ice clouds is given. These results are presented in Table 2. For the clouds that have mean depolarization values greater than 10%, the AERI phase algorithm reports mixed-phase or ice clouds approximately 80% of the time. For clouds that might be considered to be liquid water clouds through analysis from only the DABUL's depolarization values, the AERI phase algorithm classifies the clouds as liquid water 50% of the time. These values indicate that the AERI phase algorithm has considerable skill in determining cloud phase for single-layer clouds.

The cloud phase statistics determined by the AERI were averaged to provide monthly statistics for the SHEBA experiment; these results are presented in Table 3. The results indicate that December, January, and February were considerably less cloudy than the other months. These statistics also indicate that the frequency of water, mixed-phase, and ice clouds is almost identical for the months from December through February, but that the percentage of opaque clouds, which is at a minimum in December, increases to 30% by February. Ice clouds are more prevalent in November and April, and liquid water clouds are more dominant in May.

A monthly breakdown of the DABUL data, which is consistent with Intrieri et al. (2002), is provided in Table 4, which provides an alternative mechanism for evaluating the AERI phase determination algorithm. Note that significantly less data were collected during February, because the lidar was offline for repair. These results show that the clear-sky fraction is slightly overestimated by the AERI method as compared to the lidar. This overestimation is due to the cloud detection routine used by the AERI phase algorithm, which requires that the cloud have an effective emissivity of at least 5% at 900 cm^{-1}. Therefore, this technique falsely classifies very thin clouds (typically higher cirrus clouds) as clear sky. Tables 3 and 4 also suggest that the majority of the clouds classified as opaque by the AERI algorithm from March through May are liquid water clouds, because the sum of the opaque and liquid water fractions is approximately the same as the fraction where the lidar's depolarization is less than 10%.

TABLE 4. Monthly statistics on the number of hours of data collected by the DABUL during SHEBA that were either reported as clear or had a single cloud layer. The cases that had only a single cloud layer were then separated into bins with mean depolarization values of less than 10%, between 10% and 30%, and over 30%. Note that the lidar was offline for repair for a large part of Feb.

Month	Hours	Clear	Depolarization $< 10\%$	$10\% <$ depolarization $< 30\%$	Depolarization $> 30\%$
Nov	461.2	36%	19%	30%	15%
Dec	536.7	65%	6%	20%	9%
Jan	663.3	59%	19%	15%	8%
Feb	44.3	59%	41%	0%	0%
Mar	517.5	29%	46%	17%	8%
Apr	526.2	20%	51%	21%	8%
May	387.2	10%	76%	10%	4%
Total	3136.4	39%	34%	18%	9%

6. Conclusions

We have developed an algorithm that takes advantage of the differing refractive indices of ice and liquid water between 11 and 18 μm to determine cloud phase. The algorithm applies a set of tests to the emissivity spectrum calculated from high-spectral-radiance observations made by the ground-based AERI. This algorithm has been shown to accurately determine the phase of clouds independent of how the cloud particles are mixed (as either adjacent layers or uniformly mixed in the same volume). The phase retrieval algorithm is relatively insensitive to the effective size of the ice particles; however, it is slightly sensitive to the effective size of the water particles. This algorithm has been applied to downwelling radiance data collected by the AERI during the SHEBA experiment. Comparisons of the phase determination algorithm with the data from a polarization-sensitive lidar confirm the results from the simulations, with 80% of the cases where the lidar identified a single-layer cloud with a mean cloud depolarization above 10% identified as mixed-phase or ice-only by the phase determination algorithm. This algorithm has demonstrated skill at determining cloud phase using ground-based IR observations in the Arctic.

We plan on extending the algorithm to utilize more spectral channels in both the 8–13-μm and 17–25-μm windows to improve these retrievals. Furthermore, the cloud boundary information from either cloud radar or lidar observations will be used for the retrieval of both the ice water path (IWP) and liquid water path (LWP) for all cases where the optical depth is below approximately 5. These data will then be used to build daily and monthly mean climatologies of cloud phase at the ARM site in Barrow. The algorithm could also be used to ascertain cloud phase during the dry winter months at midlatitude locations, such as the ARM SGP site in Oklahoma.

Acknowledgments. DABUL data were retrieved from the UCAR JOSS archive. We thank Janet Intrieri for the helpful discussions regarding the interpretation of these data, as well as for the high-temporal-resolution lidar data presented in the case studies. Bob Knuteson provided many helpful discussions regarding the calibration of the AERI, as well as insightful comments on an earlier draft of this paper. We appreciate the helpful suggestions from three anonymous reviewers. This work was conducted as part of the ARM Program sponsored by the U.S. Department of Energy, Office of Energy Research, Office of Health and Environmental Research, Environmental Sciences Division.

REFERENCES

Alvarez, R. J., W. L. Eberhard, J. M. Intrieri, C. J. Grund, and S. P. Sandberg, 1998: A depolarization and backscatter lidar for unattended operation in varied meteorological conditions. Preprints, *10th Symp. on Meteorological Observations and Instrumentation,* Phoenix, AZ, Amer. Meteor. Soc., 140–144.

Baran, A. J., and S. Havemann, 1999: Rapid computation of the optical properties of hexagonal columns using complex angular momentum theory. *J. Quant. Spectrosc. Radiat. Transfer,* **63,** 499–519.

Baum, B. A., P. F. Soulen, K. I. Strabala, M. D. King, S. A. Ackerman, W. P. Menzel, and P. Yang, 2000: Remote sensing of cloud properties using MODIS airborne simulator imagery during SUCCESS. 2. Cloud thermodynamic phase. *J. Geophys. Res.,* **105,** 11 781–11 792.

Bohren, C. F., and D. R. Huffman, 1983: *Absorption and Scattering of Light by Small Particles.* John Wiley and Sons, 530 pp.

Campbell, J. R., D. L. Hlavka, E. J. Welton, C. J. Flynn, D. D. Turner, J. D. Spinhirne, V. S. Scott, and I. H. Hwang, 2002: Full-time, eye-safe cloud and aerosol lidar observations at Atmospheric Radiation Measurement Program sites: Instruments and data processing. *J. Atmos. Oceanic Technol.,* **19,** 431–442.

Clough, S. A., and M. J. Iacono, 1995: Line-by-line calculations of atmospheric fluxes and cooling rates: Application to carbon dioxide, ozone, methane, nitrous oxide, and the halocarbons. *J. Geophys. Res.,* **100,** 16 519–16 535.

——, ——, and J. L. Moncet, 1992: Line-by-line calculations of atmospheric fluxes and cooling rates: Application to water vapor. *J. Geophys. Res.,* **97,** 15 761–15 785.

Curry, J. A., W. B. Rossow, D. Randall, and J. L. Schramm, 1996: Overview of Arctic cloud and radiation characteristics. *J. Climate,* **9,** 1731–1764.

Daniel, J. S., S. Solomon, R. W. Portmann, A. O. Langford, C. S. Eubank, E. G. Dutton, and W. Madeson, 2002: Cloud liquid water and ice measurements from spectrally resolved near-infrared observations: A new technique. *J. Geophys. Res.,* **107,** 4599, doi: 10.1029/2001JD000688.

Downing, H. D., and D. Williams, 1975: Optical constants of water in the infrared. *J. Geophys. Res.,* **80,** 1656–1661.

Huang, H.-L., X. Wu, J. Li, P. Antonelli, R. O. Knuteson, E. R. Olson,

K. C. Baggett, and B. J. Osborne, 2001: Simultaneous retrieval of cloud height and effective emissivity from hyperspectral radiance measurements. Preprints, *11th Conf. on Satellite Meteorology and Oceanography,* Madison, WI, Amer. Meteor. Soc., 500–503.

Intrieri, J. M., M. D. Shupe, T. Uttal, and B. J. McCarty, 2002: An annual cycle of Arctic cloud characteristics observed by radar and lidar at SHEBA. *J. Geophys. Res.,* **107,** 8030, doi:10.1029/2000JC000423.

Key, J. R., and J. M. Intrieri, 2000: Cloud particle phase determination with the AVHRR. *J. Appl. Meteor.,* **39,** 1797–1804.

Knap, W. H., P. Stammes, and R. B. A. Koelemeijer, 2002: Cloud thermodynamic-phase determination from near-infrared spectra of reflected sunlight. *J. Atmos. Sci.,* **59,** 83–96.

Lawson, R. P., B. A. Baker, C. G. Schmitt, and T. L. Jensen, 2001: An overview of microphysical properties of Arctic clouds observed in May and July 1998 during FIRE.ACE. *J. Geophys. Res.,* **106,** 14 989–15 014.

Minnett, P. J., R. O. Knuteson, F. A. Best, B. J. Osborne, J. A. Hanafin, and O. B. Brown, 2001: The Marine-Atmospheric Emitted Radiance Interferometer: A high-accuracy, seagoing infrared spectrometer. *J. Atmos. Oceanic Technol.,* **18,** 994–1013.

Mishchenko, M. I., J. W. Hovenier, and L. D. Travis, Eds., 2000: *Light Scattering by Nonspherical Particles: Theory, Measurements, and Applications.* Academic Press, 690 pp.

Moran, K. P., B. E. Martner, M. J. Post, R. A. Kropfli, D. C. Welsh, and K. B. Widener, 1998: An unattended cloud-profiling radar for use in climate research. *Bull. Amer. Meteor. Soc.,* **79,** 443–455.

Nakamura, N., and A. H. Oort, 1988: Atmospheric heat budgets of the polar regions. *J. Geophys. Res.,* **93,** 9510–9524.

Pilewskie, P., and S. Twomey, 1987a: Cloud phase discrimination by reflectance measurements near 1.6 and 2.2 μm. *J. Atmos. Sci.,* **44,** 3419–3421.

——, and ——, 1987b: Discrimination of ice from water in clouds by optical remote sensing. *Atmos. Res.,* **21,** 113–122.

Revercomb, H. E., H. Buijs, H. B. Howell, D. D. LaPorte, W. L. Smith, and L. A. Sromovsky, 1988: Radiometric calibration of the IR Fourier transform spectrometers: Solution to a problem with the High-Resolution Interferometer Sounder. *Appl. Opt.,* **27,** 3210–3218.

——, F. A. Best, R. G. Dedecker, T. P. Dirkx, R. A. Herbsleb, R. O. Knuteson, J. F. Short, and W. L. Smith, 1993: Atmospheric Emitted Radiance Interferometer (AERI) for ARM. Preprints, *Fourth Symp. on Global Climate Change Studies,* Anaheim, CA, Amer. Meteor. Soc., 46–49.

Rossow, W. B., and R. A. Schiffer, 1999: Advances in understanding clouds from ISCCP. *Bull. Amer. Meteor. Soc.,* **80,** 2261–2287.

Sassen, K., 1991: The polarization lidar technique for cloud research: A review and current assessment. *Bull. Amer. Meteor. Soc.,* **72,** 1848–1866.

Sekelsky, S., and R. McIntosh, 1996: Cloud observations with a polarimetric 33 GHz and 95 GHz radar. *Meteor. Atmos. Phys.,* **59,** 123–140.

Serreze, M. C., R. G. Barry, and J. E. Walsh, 1995: Atmospheric water vapor characteristics at 70°N. *J. Climate,* **8,** 719–731.

Smith, W. L., R. O. Knuteson, H. E. Revercomb, F. Best, R. Dedecker, and H. B. Howell, 1993: GB-HIS: A measurement system for continuous profiling of the boundary layer thermodynamic structure. Preprints, *Eighth Symp. on Meteorological Observations and Instruments,* Anaheim, CA, Amer. Meteor. Soc., J180–J183.

Stamnes, K., S.-C. Tsay, W. Wiscombe, and K. Jayaweera, 1988: A numerically stable algorithm for discrete-ordinate-method radiative transfer in multiple scattering and emitting layered media. *Appl. Opt.,* **27,** 2502–2509.

——, R. G. Ellingson, J. A. Curry, J. E. Walsh, and B. D. Zak, 1999: Review of science issues, deployment strategy, and status of the ARM North Slope of Alaska–Adjacent Arctic Ocean climate research site. *J. Climate,* **12,** 46–63.

Strabala, K. I., S. A. Ackerman, and W. P. Menzel, 1994: Cloud properties inferred from 8–12-μm data. *J. Appl. Meteor.,* **33,** 212–229.

Sun, Z., and K. P. Shine, 1995: Parameterization of ice cloud radiative properties and its application to the potential climatic importance of mixed-phase clouds. *J. Climate,* **8,** 1874–1888.

Tobin, D. C., and Coauthors, 1999: Downwelling spectral radiance observations at the SHEBA ice station: Water vapor continuum measurements from 17 to 26 μm. *J. Geophys. Res.,* **104,** 2081–2092.

Turner, D. D., B. M. Lesht, S. A. Clough, J. C. Liljegren, H. E. Revercomb, and D. C. Tobin, 2003: Dry bias and variability in Vaisala RS80-H radiosondes: The ARM experience. *J. Atmos. Oceanic Technol.,* **20,** 117–132.

Uttal, T., and Coauthors, 2002: Surface heat budget of the Arctic Ocean. *Bull. Amer. Meteor. Soc.,* **83,** 255–276.

Wang, J., H. L. Cole, D. J. Carlson, E. R. Miller, and K. Beierle, 2002: Corrections of humidity measurement errors from the Vaisala RS80 radiosonde—Application to TOGA COARE data. *J. Atmos. Oceanic Technol.,* **19,** 981–1002.

Warren, S., 1984: Optical constants of ice from the ultraviolet to the microwave. *Appl. Opt.,* **23,** 1206–1225.

Yang, P., and K. N. Liou, 1996: Geometric-optics-integral-equation method for light scattering by nonspherical ice crystals. *Appl. Opt.,* **35,** 6568–6584.

——, ——, M. I. Mishchenko, and B. C. Gao, 2000: Efficient finite-difference time-domain scheme for light scattering by dielectric particles: Application to aerosols. *Appl. Opt.,* **39,** 3727–3737.

——, B. C. Gao, B. A. Baum, Y. X. Hu, W. J. Wiscombe, S. C. Tsay, D. M. Winker, and S. L. Nasiri, 2001: Radiative properties of cirrus clouds in the infrared (8–13 μm) spectral region. *J. Quant. Spectrosc. Radiat. Transfer,* **70,** 473–504.